Journal of Stress Analysis
Vol. 2, No. 2, Autumn – Winter 2017-18
Bu-Ali Sina University

Ductile Fracture Analysis of High-strength Steel Bars Using Micromechanical GTN Model

H. Bahrami Ghalehjoogh, S.H. Hoseini*
Mechanical Engineering Department, Urmia University of Technology, Urmia, Iran.

Article info

Article history:
Received 08 January 2018
Received in revised form
04 March 2018
Accepted 04 March 2018

Keywords:
Ductile fracture
Gurson-Tvergaard-Needleman model
Damage
High-strength steel

Abstract

Recent studies on the mechanics of materials have shown that the ductile fracture is significantly affected by the stress invariants among progressive plastic deformation. In this paper the micro-mechanical Gurson-Tvergaard-Needleman (GTN) model is utilized to investigate the fracture behavior of high-strength steel AISI 4340 under various stress triaxialities. Experimental tensile tests were conducted on the smooth and notched round-bar specimens to evaluate the effect of the stress triaxiality on the fracture initiation. Subsequently, finite element (FE) simulations were implemented using Abaqus/Explicit via the user subroutine VUMAT. The comparison between the simulations and experimental results indicate the best accuracy of the GTN micromechanical model to appraise the ductile fracture initiation. Furthermore, the results demonstrate the significant effect of the stress triaxiality value on the start of the ductile rupture.

Nomenclature

σ	Stress tensor	s	Deviatoric stress tensor
σ_m	Mean stress	σ_{eq}	Von-Mises equivalent stress
σ_Y	Flow stress	σ_0	Initial yield stress of the matrix material
f^*	Effective void volume fraction	f_0	Initial void volume fraction
f	Void volume fraction	f_c	Critical void volume fraction
f_f	Failure void volume fraction at the onset of fracture	ε_N	Mean value of the plastic strain for void nucleation
F_N	Volume fraction of void nucleating particles	ε_m	Effective matrix plastic strain
S_N	Standard deviation	ε	Total strain tensor
ε^{el}	Elastic strain tensor	ε^{pl}	Plastic strain tensor
$\mathbb{C}$	Fourth order isotropic elasticity tensor	$\mathbf{I}$	Identity tensor
ϕ	Yield function	q_i	Tvergaard parameters
R	Residual function	E	Elasticity modulus
Q_i	Voce hardening parameters	v	Poisson's ratio
:	Double dot product		

1. Introduction

The fracture phenomenon in materials has attracted a large amount of attention during the last decades. The significance of predicting fracture in engineering materials, especially metallic alloys, has increased with further industrial development. Therefore an enormous

*Corresponding author: S.H. Hoseini (Assistant Professor)
E-mail address: s.hamedhoseini@uut.ac.ir
http://dx.doi.org/10.22084/jrstan.2018.15463.1039
ISSN: 2588-2597

number of studies have been conducted to estimate the fracture behavior of materials in macro and micro scales. In micro-scale, the ductile fracture can be explained by three separate phases, including nucleation of micro-voids, growth of existing voids and finally, coalescence of them. Studies on the nucleation, growth, and coalescence of voids were initially conducted by McClintock in 1968 [1] and Rice and Tracey in 1969 [2]. They proposed relations for the growth of the voids by considering the growth of a cylindrical or spherical void in an infinite rigid perfect plastic matrix subjected to remote stress fields. The sensitivity of the void growth to the stress triaxiality was detected in both models. Stress triaxiality is defined as the ratio of the hydrostatic stress to the von Mises equivalent stress. The deficiency of the mentioned models was the incapability of them to take into account the void interaction and also void growth effects on the material behavior. These problems were considered in 1977 by Gurson [3]. He studied the plastic flow in a finite sphere, including a spherical void and proposed a yield function for a porous-like material, including both of the void interaction and growth effects. In order to better reflect the effect of the void interaction, Tvergaard [4] improved the Gursons model by incorporating extra parameters. The Gurson's model and its modification proposed by Tvergaard were not able to explain the rapid loss of strength at the onset of the fracture. Therefore, Tvergaard and Needleman [5] enhanced the former model by including void coalescence effects. This model is well-known as Gurson-Tvergaard-Needleman (GTN). The GTN model only contains the first and second stress invariants. The lack of the third stress invariant is a weakness for this model especially when the stress triaxiality is low and shear becomes the dominant mechanism in the failure. Consequently, Xue [6] and Nashon and Hutchinson [7] proposed modifications to the GTN model by adding the third stress invariant effects on the fracture behavior of the material. Concurrently, various studies were conducted to investigate the effects of the second and third stress invariants by experiments and numerical simulations [8-17]. Bao and Wierzbicki [8] performed some experimental tests on aluminum alloys in a wide range of stress triaxialities to estimate their effects on the fracture strain. Bonora et al. [9] and Mirone [10] carried out some experimental tests on the smooth and notched specimens and demonstrated that ductile failure is remarkably influenced by different stress triaxiality regimes. Barsoum and Faleskog [11,12] and Brunig et al. [13] studied the ductile failure dependence on the stress triaxiality as well as the Lode angle parameter and showed that the Lode angle has a significant effect on the ductile fracture initiation. Bai and Wierzbicki [14] proposed a new metal plasticity model incorporating all stress invariants. This model that predicts the material behavior up to fracture initiation is established based on the stress triaxiality and Lode angle parameters. Driemeier et al. [15] designed modified Arcan specimens to examine the effect of rapid changes in stress states and deformation modes on the behavior of a kind of aluminum alloy. Khan and Liu [16] conducted experimental tests in a wide range of stress triaxialities to establish an empirical ductile fracture criterion for engineering applications. Malcher et al. [17] considered three constitutive models, including Xue [6], Lemaitre [18] and Bai and Wierzbicki [14] models to compare their applicability and prediction reliability under a wide range of stress triaxialities. More recently, the effect of the stress triaxility and the Lode angel parameter were reported by many researchers [19-22]. In this study experimental tensile tests were carried out on the smooth and notched round-bar samples of high strength AISI 4340 steel. Notched round-bar specimens with different notch radii were utilized to capture the material behavior under increasing stress triaxialities. Numerical simulations were implemented based on the GTN model, and the simulation results were compared with the experimental ones. Results show the accuracy of the GTN model to predict the ductile fracture under various stress triaxialities.

2. Governing Equations

As mentioned in the introduction section, one of the most widely used micro-mechanical models which describes the ductile fracture behavior of materials is the GTN model. The GTN model takes into account the void nucleation, growth and coalescence stages. The yield function ϕ, based on the GTN model is represented as [5]:

$$\phi = \frac{\sigma_{eq}^2}{\sigma_Y^2} + 2q_1 f^* \cosh\left(\frac{3q_2\sigma_m}{2\sigma_Y}\right) - [1 + q_3 f^{*2}] = 0 \tag{1}$$

In the equation above, $\sigma_{eq} = \sqrt{\frac{3}{2}\mathbf{s} : \mathbf{s}}$ is the equivalent von Mises stress where $\mathbf{s}$ denotes the devatoric part of stress tensor. The symbol (:) shows double dot product between two tensors and $\sigma - m = \frac{1}{3}\sigma : \mathbf{I}$ is the hydrostatic part of the stress tensor where $\mathbf{I}$ denotes second order identity tensor. σ_Y is the flow stress of the matrix material which follows a von Mises yield criterion. q_1, q_2, and q_3 are Tvergaard parameters [4]. f^* is the effective void volume fraction proposed by Tvergaard and Needleman [5] to incorporate the coalescence effect of voids and is defined as:

$$\begin{aligned} f^*(f) &= f && f < f_c \\ f^*(f) &= f_c + \frac{\frac{1}{q_1} - f_c}{f_f - f_c}(f - f_c) && f_c \le f \le f_f \end{aligned} \tag{2}$$

where f_c and f_f are critical and failure void volume fractions, respectively. Voids start to show coalescence in the material when the void volume fraction reaches f_c and the material fails when it becomes equal to f_f. Note that if $f = 0$, Eq. 1 decreases to von Mises yield function. The GTN model assumes that the void growth rate is a result of the nucleation of secondary voids and growth of existing voids [5].

$$\dot{f} = \dot{f}_{\text{nucleation}} + \dot{f}_{\text{growth}} \tag{3}$$

The nucleation term is assumed to be plastic strain controlled and was proposed by Chu and Needleman [23] as:

$$\dot{f}_{\text{nucleation}} = A_N \dot{\varepsilon}_M \tag{4}$$

$$A_N = \frac{F_N}{S_N\sqrt{2\pi}} \exp\left[-\frac{1}{2}\left(\frac{\varepsilon_M - \varepsilon_N}{S_N}\right)^2\right] \tag{5}$$

where F_N, ε_N, and S_N are the volume fraction of void nucleating particles, mean value of plastic strain for void nucleation and standard deviation, respectively. ε_M is the effective matrix plastic strain and its growth rate is given as:

$$\dot{\varepsilon}_M = \sqrt{\frac{2}{3}\dot{\varepsilon}^{pl} : \dot{\varepsilon}^{pl}} \tag{6}$$

where $\dot{\varepsilon}^{pl}$ denotes the plastic strain tensor. The rate of the effective matrix plastic strain can be written according to the equivalency of the overall rate of macroscopic and microscopic plastic work as [5]:

$$\dot{\varepsilon}_M = \frac{\sigma : \dot{\varepsilon}^{pl}}{(1-f)\sigma_Y} \tag{7}$$

Also the growth rate of voids is defined as:

$$\dot{f}_{\text{growth}} = (1-f)tr(\dot{\varepsilon}^{pl}) \tag{8}$$

where $tr(\dot{\varepsilon}^{pl})$ is the trace of the plastic strain rate tensor.

3. Numerical Implementation

To implement the GTN model, a numerical procedure based on the return mapping algorithm was proposed. The algorithm was implemented in Abaqus/Explicit via the user subroutine VUMAT. According to this method, all variables were discretized based on the backward Euler method. All variables were assumed to be given at the start of an increment, which is shown by subscript n, then by using return mapping algorithm, the variables were evaluated at the end of the increment, which is shown by subscript $n+1$. Considering the interval from the state n to $n+1$, the backward Euler method allows to discretize the constitutive equations as:

$$\epsilon_{n+1} = \epsilon^{el}_{n+1} + \epsilon^{pl}_{n+1} \tag{9}$$

$$\epsilon_{n+1} = \epsilon_n + \Delta\epsilon \tag{10}$$

$$\sigma_{n+1} = \sigma_n + \mathbb{C} : (\Delta\epsilon - \Delta\epsilon^p) \tag{11}$$

where $\mathbb{C}$ is the fourth-order isotropic elasticity; ϵ and ϵ^{el} denote the total strain and elastic strain tensors, respectively. By supposing that the strain increment given in end of the increment is completely elastic, the stress tensor, which is known as the trial stress tensor, can be calculated as:

$$\sigma^{\text{trial}} = \sigma - n + \mathbb{C} : \Delta\epsilon \tag{12}$$

Consequently, the corresponding yield function $\phi(\sigma_m^{\text{trial}} \cdot \sigma_{eq}^{\text{trial}} \cdot H_{i_n})$ can be obtained, where H_i $(i = 1, 2)$ represents scalar state variables f and respectively. If $\phi \leq 0$ yielding does not occur in this increment and current state is elastic. This means that the response is elastic and the trial stress and other constitutive variables come to be the final stress and the constitutive variables at this increment, thus:

$$\sigma_{n+1} = \sigma^{\text{trial}} \tag{13}$$

Otherwise, if $\phi > 0$ the current state is plastic and Eq. 13 is no longer valid. Therefore, the plastic correction should be determined using Newton-Raphson iterative method. The incremental form of the plastic strain tensor can be written in the form of its spherical and deviatoric parts as:

$$\Delta\epsilon^p = \frac{1}{3}\Delta e_m \mathbf{I} + \Delta\epsilon_q \mathbf{n}_{n+1} \tag{14}$$

where

$$\mathbf{n}_{n+1} = \frac{3}{2}\frac{\mathbf{S}_{n+1}}{\sigma_{eq}} \tag{15}$$

$$\Delta\epsilon_m = \Delta\lambda\left(\frac{\partial\phi}{\partial\sigma}\right) \tag{16}$$

$$\Delta\epsilon_q = \Delta\lambda\left(\frac{\partial\phi}{\partial\sigma_{eq}}\right) \tag{17}$$

Eliminating $\Delta\lambda$ from equations (16) and (17) gives a residual function as:

$$R = \Delta\epsilon_m\left(\frac{\partial\phi}{\partial\sigma_{eq}}\right) - \Delta\epsilon_q\left(\frac{\partial\phi}{\partial\sigma_m}\right) = 0 \tag{18}$$

Newton-Raphson iterative method should be utilized to solve the non-linear Eq. 18 and $\phi(\sigma_m \cdot \sigma_{eq} \cdot H_i)$. This iterative method continues until the values of $\Delta\epsilon_q$ and $\Delta\epsilon_m$ and consequently Newton-Raphson method converge. The convergence criteria were selected such that the value of R and ϕ became almost zero. In this work, the tolerance value was assumed 10^{-6}. Therefore by using the converged values of $\Delta\epsilon_q$ and $\Delta\epsilon_m$ the stress tensor and state variables can be updated at the end of the increment. The stress integration flow chart is represented in Fig. 1.

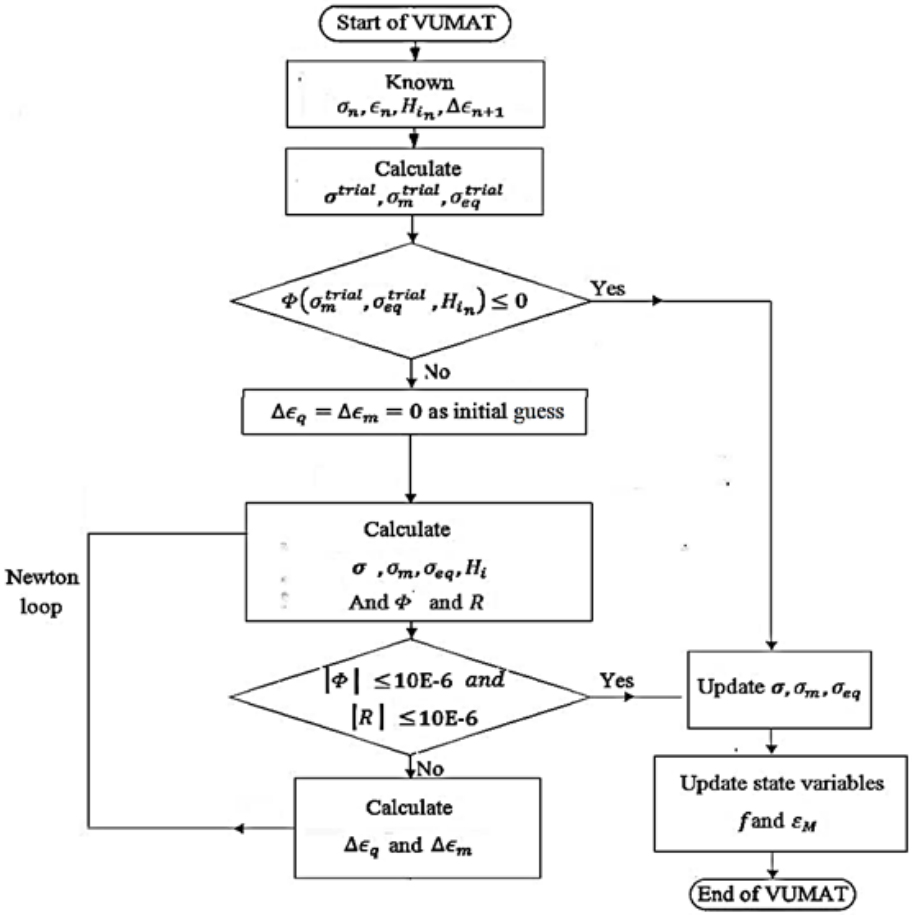

Fig. 1. VUMAT subroutine flow chart for GTN model.

4. Experimental Procedure

To evaluate the GTN model, a series of experimental tests were carried out on the three types of test specimens. These test specimens were the smooth round-bars and the notched round-bars with medium and sharp notch radiuses which were designed and prepared based on the Bao and Wierzbicki work [24]. All samples were made of AISI 4340 high strength steel with a total length of 120mm. Geometry of each specimen is illustrated in Fig. 2. Three specimens were implemented for each type of the experimental test and the average of the results was represented as an experimental curve. Fig. 3 represents the experimental force-displacement curves of the smooth samples. Extension of the specimens were measured using an extensometer with a gauge length of 12.5mm for the smooth and sharp notched bars and with a gauge length of 25mm for the medium notched bars. All tests were conducted at room temperature and in a strain rate of 0.5mm/min. Fig. 4 shows the specimens which were firmly clamped by the grippers of a 30-ton capacity Instron servo-hydraulic machine. The SEM images of the fracture surface of the specimens are shown in Figs. 5-7. The cup and cone type of fracture surface as well as the micro-dimple patterns can be observed. Near outer surface, the dense of the dimples are less than the center of specimen. This feature shows that the hydrostatic stress has a significant effect on the nucleation and growth of the micro-voids.

5. FEM Simulations

In this section the numerical simulations of the tested specimens are presented. The matrix material was assumed to obey a two-term Voce hardening relation as represented in the following equation:

$$\sigma_Y = \sigma_0 + Q_1(1 - \exp(-b_1\varepsilon_M)) + Q_2(1 - \exp(-b_2\varepsilon_M)) \tag{19}$$

where Q_i and b_i are the hardening parameters and were calibrated by the numerical simulation of the experimental tests. The calibrated parameters of AISI 4340 high-strength steel are presented in Table 1. The material parameters and also GTN dimensionless parameters used in this study were calculated based on the smooth sample and are represented in Table 2. The initial void volume fraction f_0 was assumed to be 0.0001 and the set of parameters $\{q_1 \cdot q_2 \cdot q_3 \cdot f_n \cdot S_n\}$ were chosen from the work of Narasimhan et al. [25] and $\{f_c \cdot \varepsilon_N \cdot f_f\}$ were calculated by numerical simulation fitting to experimental results by the trial and error method.

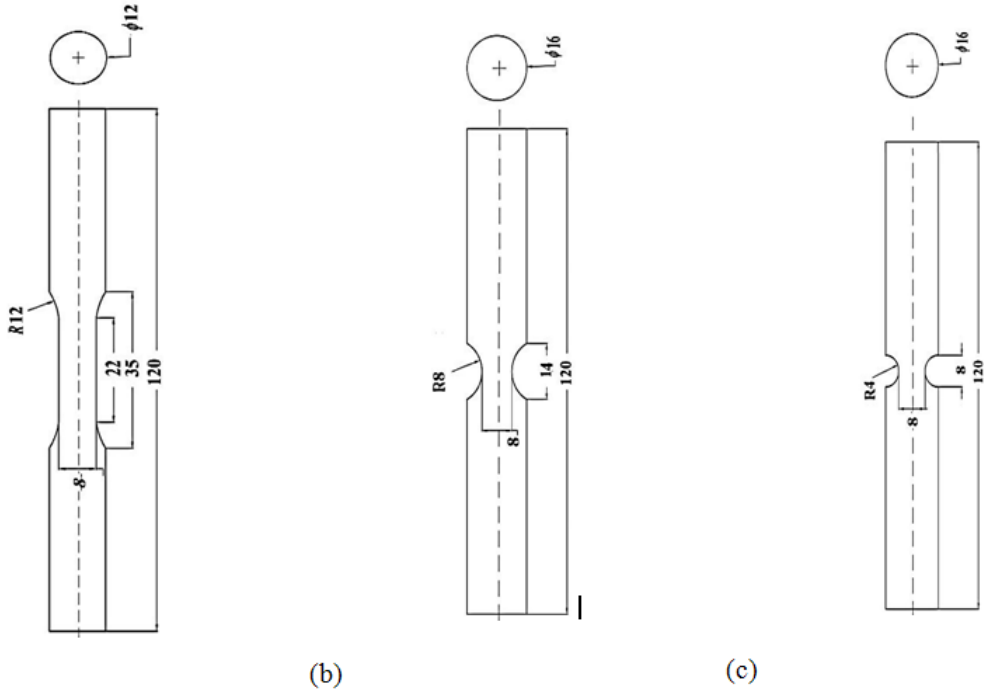

Fig. 2. Dimensions of tested specimens. (a) Smooth bar, (b) Large radius notched bar, (c) Small radius notched bar.

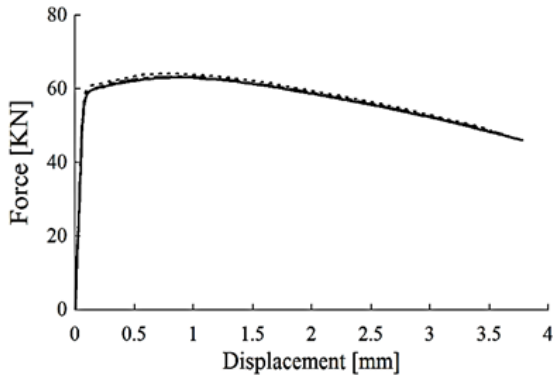

Fig. 3. Experimental force-displacement curves of the three smooth specimens.

Table 1
Hardening parameters.

Q_1	b_1	Q_2	b_1
85MPa	600	100MPa	25

5.1. Smooth Round Bar

Only a quarter of the smooth round bar was simulated using 2400 four-node axisymmetric elements with reduced integration (CAX4R in Abaqus element library), due to axis-symmetry condition as shown in Fig. 8. The boundary conditions of the FE models were defined based on the displacement condition on the specified nodes. All the nodes on the top edge were displaced in the vertical direction while the nodes on the bottom edge were constrained in that direction.

The comparison of the force-displacement curves from simulation and experiment is given in Fig. 9a. It can be seen that the numerical simulation result is in good agreement with the experiment, and the maximum value of error between simulation and experiment does not exceed 5% for the smooth specimen. Fig. 9b compares the stress-plastic strain curves between the fitted Voce hardening model and the experimental result of the smooth round bar. It shows that the two-term Voce hardening can accurately predict the plastic behavior. In this figure, the coefficient of determination, which denoted , is about 99%. Fig. 10a-d shows the contour plots of the effective matrix plastic strain at different displacements until the onset of the fracture.

As it can be seen, the distribution of the effective matrix plastic strain is uniform in Fig. 10a but it tends to concentrate in the center of specimen with increasing displacement in Fig. 10d, where the necking effect can be observed as well. The GTN model also predicts that the concentration of the effective matrix plastic strain is at the center of the smooth specimen at the onset of the fracture as shown in Fig. 10e.

Table 2
GTN parameters.

E	203GPa	q_1	1.5
σ_0	1100MPa	q_2	1
v	0.33	q_3	2.25
f_0	0.0001	ε_N	0.3
f_c	0.0025	F_N	0.0008
f_f	0.05	S_N	0.1

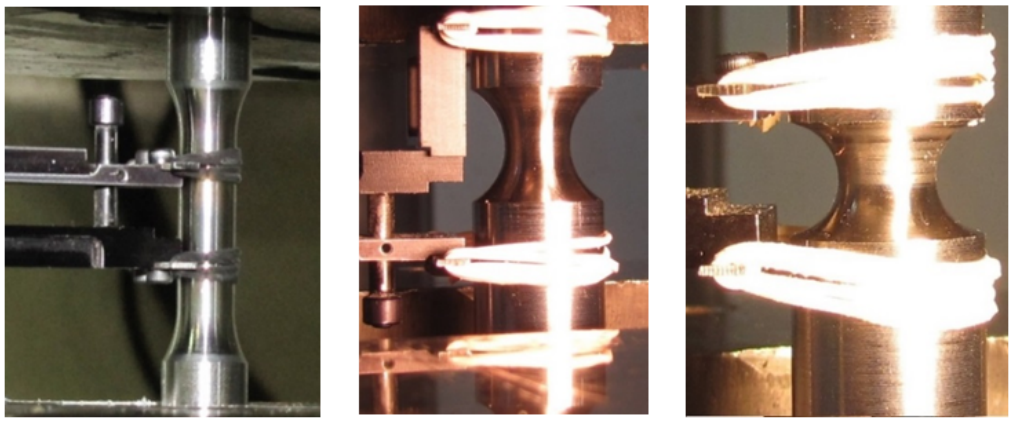

(a) (b) (c)

Fig. 4. Tested specimens. (a) Smooth bar, (b) Medium radius notched bar, (c) Sharp radius notched bar.

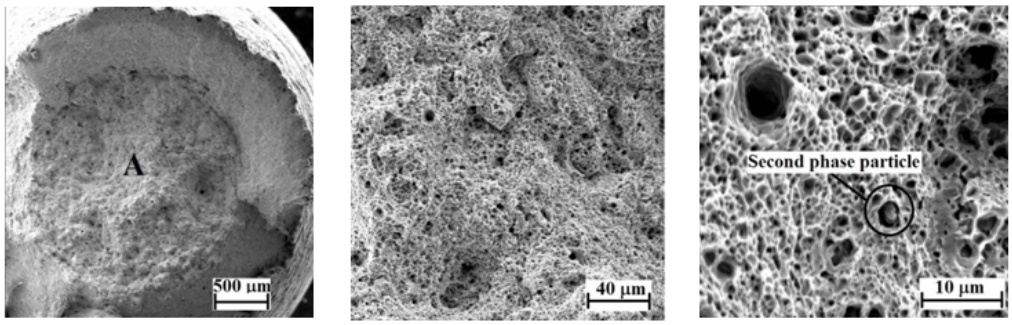

(a) (b) (c)

Fig. 5. SEM images of the fracture surface of the smooth specimen at (a) 70× magnification, (b) 1000× magnification and (c) 5000× magnification of region A respectively.

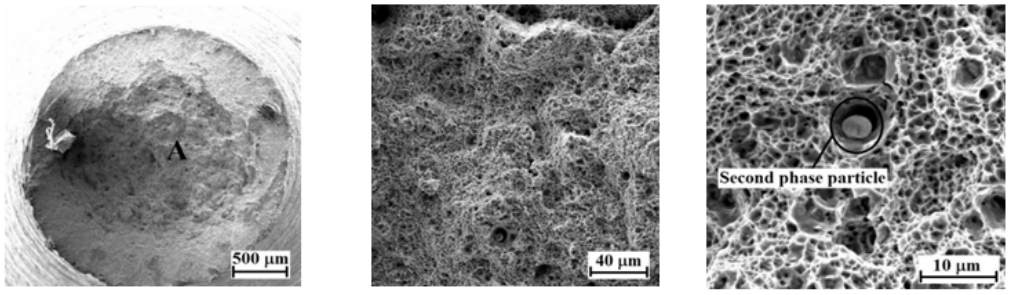

(a) (b) (c)

Fig. 6. SEM images of the fracture surface of the medium radius notched bar specimen at (a) 70× magnification, (b) 1000× magnification and (c) 5000× magnification of region A respectively.

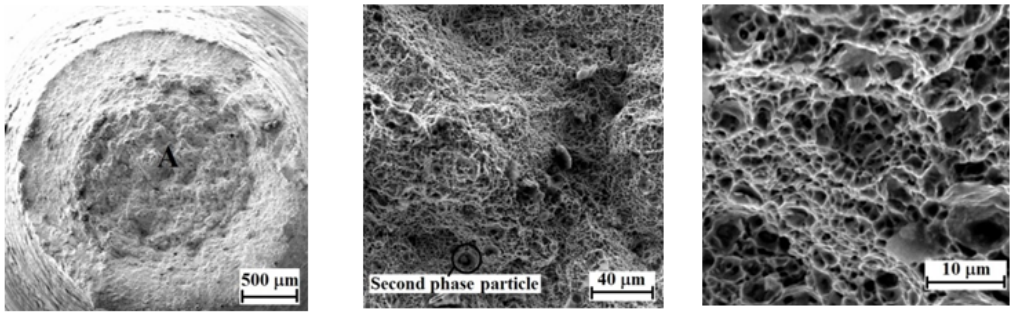

(a) (b) (c)

Fig. 7. SEM images of the fracture surface of the sharp radius notched bar specimen at (a) 70× magnification, (b) 1000× magnification and (c) 5000× magnification of region A respectively.

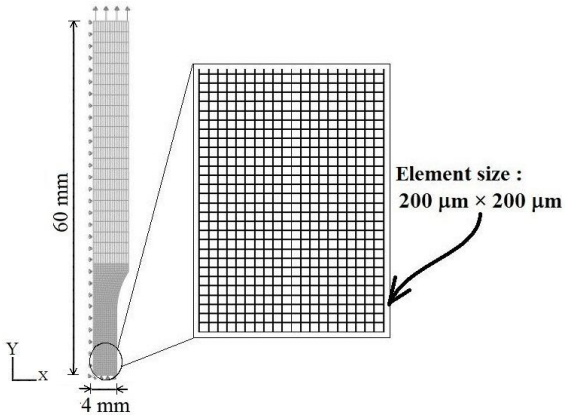

Fig. 8. Meshed model used in the finite element simulation.

Fig. 11a-d shows the contour plots of void volume fraction until the fracture initiation moment. Similar to the effective matrix plastic strain, a same tendency for increasing the displacement can be observed in the behavior of void volume fraction on the fracture surface. The GTN model predicts that the void volume fraction reaches its maximum value at the center of the fracture surface for the smooth specimen as illustrated in Fig. 11e.

It should be mentioned that both of the effective matrix plastic strain and void volume fraction curves at the onset of fracture throughout the fracture surface are in agreement with the experimental results which indicate that the fracture initiation occurs at the center of specimen.

Fig. 12a-d shows the stress triaxiality contour plots at different displacements and its concentration with increasing displacement. Fig. 12e shows the triaxiality through the fracture surface at the onset of the fracture.

5.2. Notched Round Bars

Similar to the smooth bar, a quarter of the notched round bars were modeled using four-node axisymmetric elements with reduced integration (CAX4R in Abaqus explicit) as shown in Fig. 13. The number of elements used for the large and small radius notched bars were 13160 and 12530 respectively. The material and GTN parameters of the smooth bar were used here for the notched samples too. The comparison of force - displacement curves from the simulations and experiments are given in Fig. 14. The error between the simulation and experiment does not exceed 4% for medium radius notched bar and 6% for sharp radius notched bar. As it can be seen, the ductility of the material decreases with decreasing notch radius. It can be concluded that the simulations can predict the overall behavior of force displacement curves with good agreement but it overestimates the fracture displacement in the notched bars. It is worth noting that similar to the smooth sample, the fracture initiates at the center of the specimen for the notched round-bars according to the experimental and numerical results.

The effective matrix plastic strain over the fracture surface at the onset of the fracture for the notched round-bars is shown in Fig. 15. Similar to the smooth specimen, the GTN model predicts the concentration of the effective matrix plastic strain at the center of the fracture surface for the medium radius notched bar. For the sharp radius notched bar, the simulations cannot predict the concentration of the effective matrix plastic strain at the center of the fracture surface. It can be seen from Fig. 16 that the void volume fraction growth tends to be in the center of the notched bars with increasing displacement similar to the smooth bar, and consequently, the critical value of void volume fraction occurs at the center of the fracture surface. The void volume fraction for notched round specimens increases rapidly from 0.0025 up to fracture. Consequently, the value of 0.0025 was selected as a fracture initiation void volume fraction. As a result, the location of the fracture initiation can be predicted for the smooth and medium radius notched bars using the GTN model. But unlike the smooth and medium

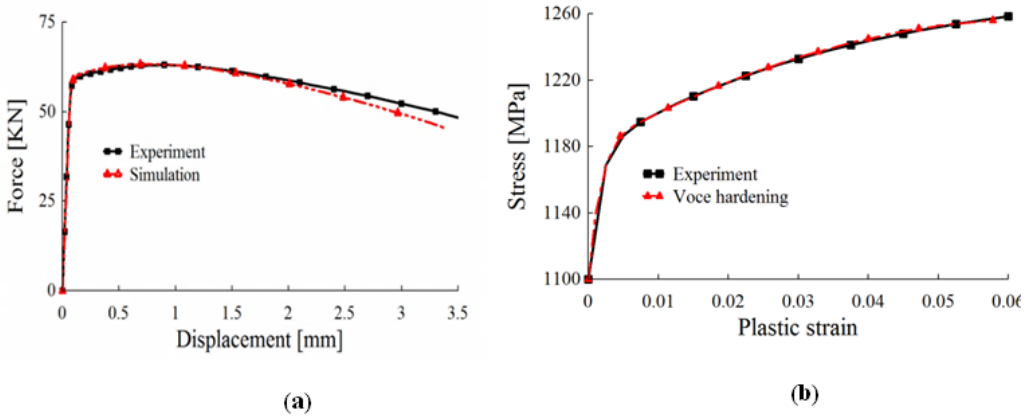

Fig. 9. a) Force displacement curves of the smooth specimen and b) Stress plastic strain curves of the smooth round bar.

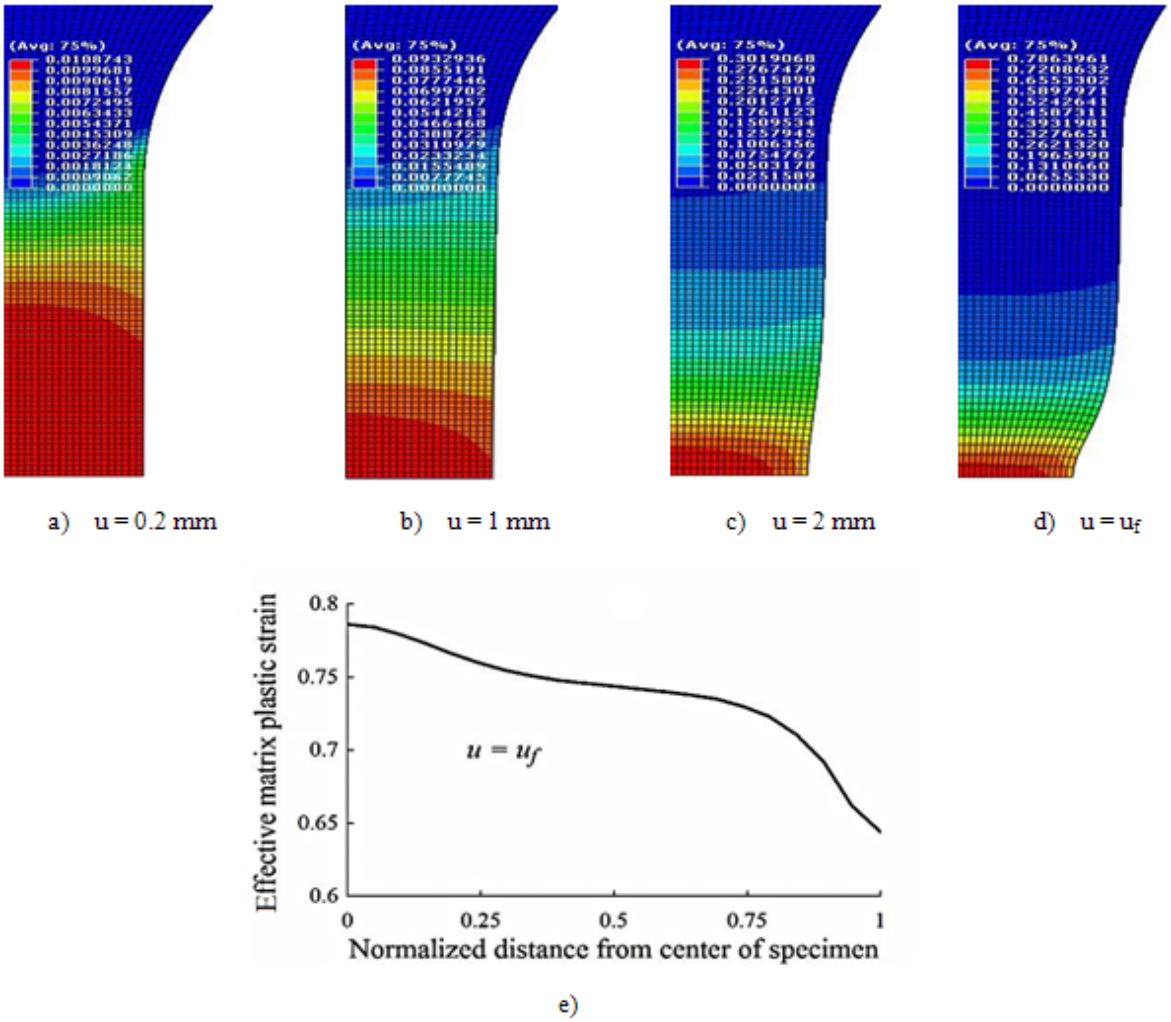

Fig. 10. a-d) Effective matrix plastic strain contours at different displacements and e) Effective matrix plastic strain over the fracture surface at the onset of fracture.

radius notched bars, the simulation cannot accurately predict the fracture onset location in the sharp radius notched bar. Similar results of the overestimation of fracture displacement and disagreement of the concentration of the effective matrix plastic strain in the notched tensile bars are also observed in the work of Malcher et al. [17] and interpreted as a result of the differences in the stress triaxialities between the notched specimen and the specimen used to calibrate the model parameters. The distribution of stress triaxiality over the fracture surface at the onset of fracture is represented in Fig. 17.

The effective matrix plastic strain over the fracture surface at the onset of the fracture for the notched round-bars is shown in Fig. 15. Similar to the smooth specimen, the GTN model predicts the concentration of the effective matrix plastic strain at the center of the fracture surface for the medium radius notched bar. For the sharp radius notched bar, the simulations cannot predict the concentration of the effective matrix plastic strain at the center of the fracture surface. It can be seen from Fig. 16 that the void volume fraction growth tends to be in the center of the notched bars with increasing displacement similar to the smooth bar, and consequently, the critical value of void volume fraction occurs at the center of the fracture surface. The void volume fraction for notched round specimens increases rapidly from 0.0025 up to fracture. Consequently, the value of 0.0025 was selected as a fracture initiation void volume fraction. As a result, the location of the fracture initiation can be predicted for the smooth and medium radius notched bars using the GTN model. But unlike the smooth and medium radius notched bars, the simulation cannot accurately predict the fracture onset location in the sharp radius notched bar. Similar results of the overestimation of fracture displacement and disagreement of the concentration of the effective matrix plastic strain in the notched tensile bars are also observed in the work of Malcher et al. [17] and interpreted as a result of the differences in the stress triaxialities between the notched specimen and the specimen used to calibrate

the model parameters. The distribution of stress triaxiality over the fracture surface at the onset of fracture is represented in Fig. 17.

6. Conclusions

In this study uniaxial tensile tests were carried out on the smooth and notched round-bar specimens made of AISI 4340 steel with various notch radii. Numerical simulations of the tested specimens were conducted using the GTN model. Good accuracy in predicting the force displacement curve of the smooth specimen was observed. For the notched specimens, the GTN model was capable of predicting the overall behavior of force - displacement curves with a good accuracy; however, it overestimates the fracture displacements. The results of the simulations show a reasonable evaluation of the effective matrix plastic strain for the smooth and large radius notched-bars. For the small radius notched bar, the effective matrix plastic strain was in disagreement with the experiments. Furthermore, the GTN model predicts that the concentration of void volume fraction rate and consequently its maximum value were at the center of specimen, which coincided with the experimental results of the smooth and also notched round bars. Therefore, it can be concluded that the GTN model can predict the fracture initiation point in the smooth and medium notched bars but for the sharp radius notched bar, this model cannot predict the fracture initiation point accurately.

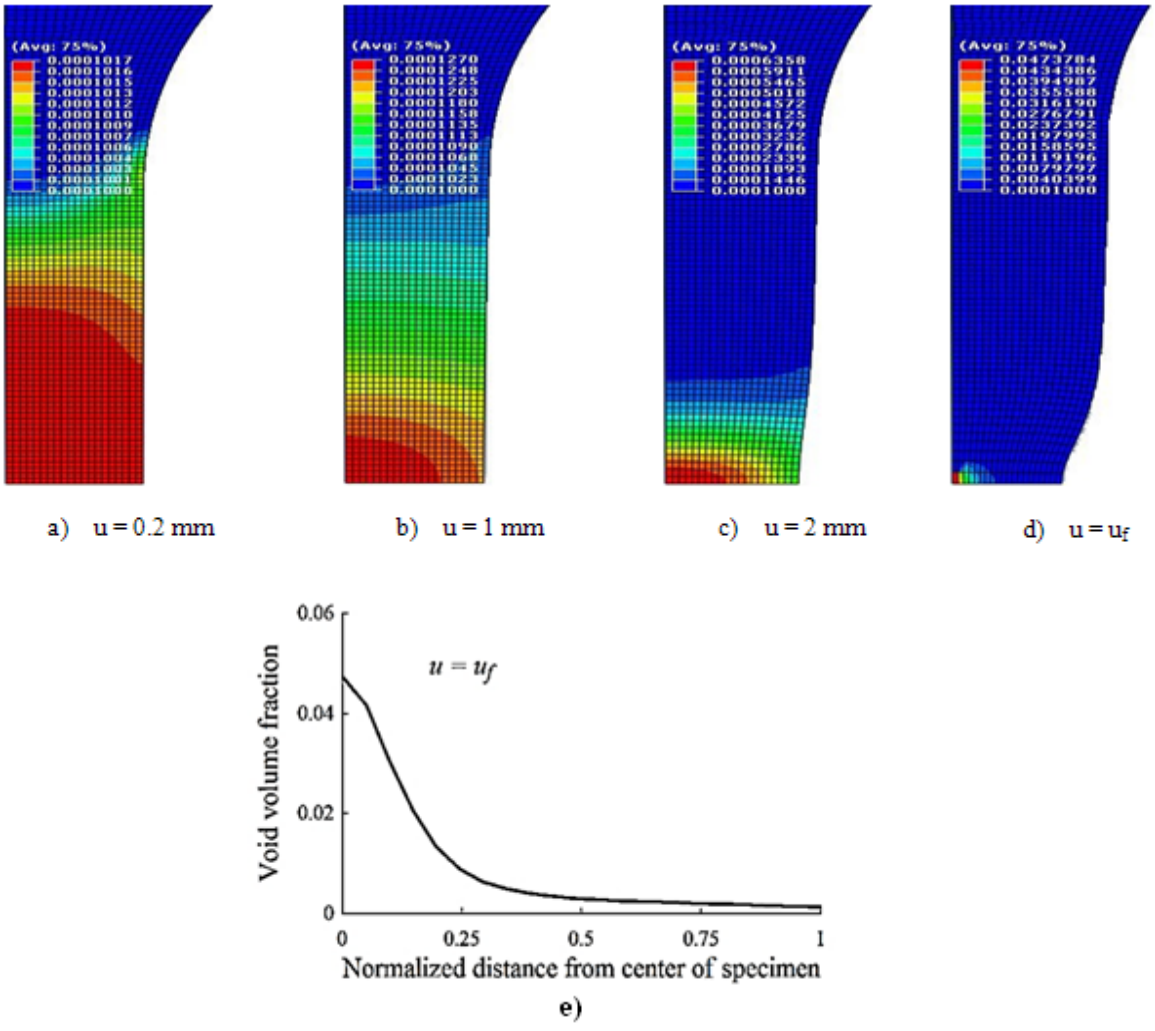

Fig. 11. a-d) Void volume fraction contours at different displacements and e) Void volume fraction over the fracture surface at the onset of fracture.

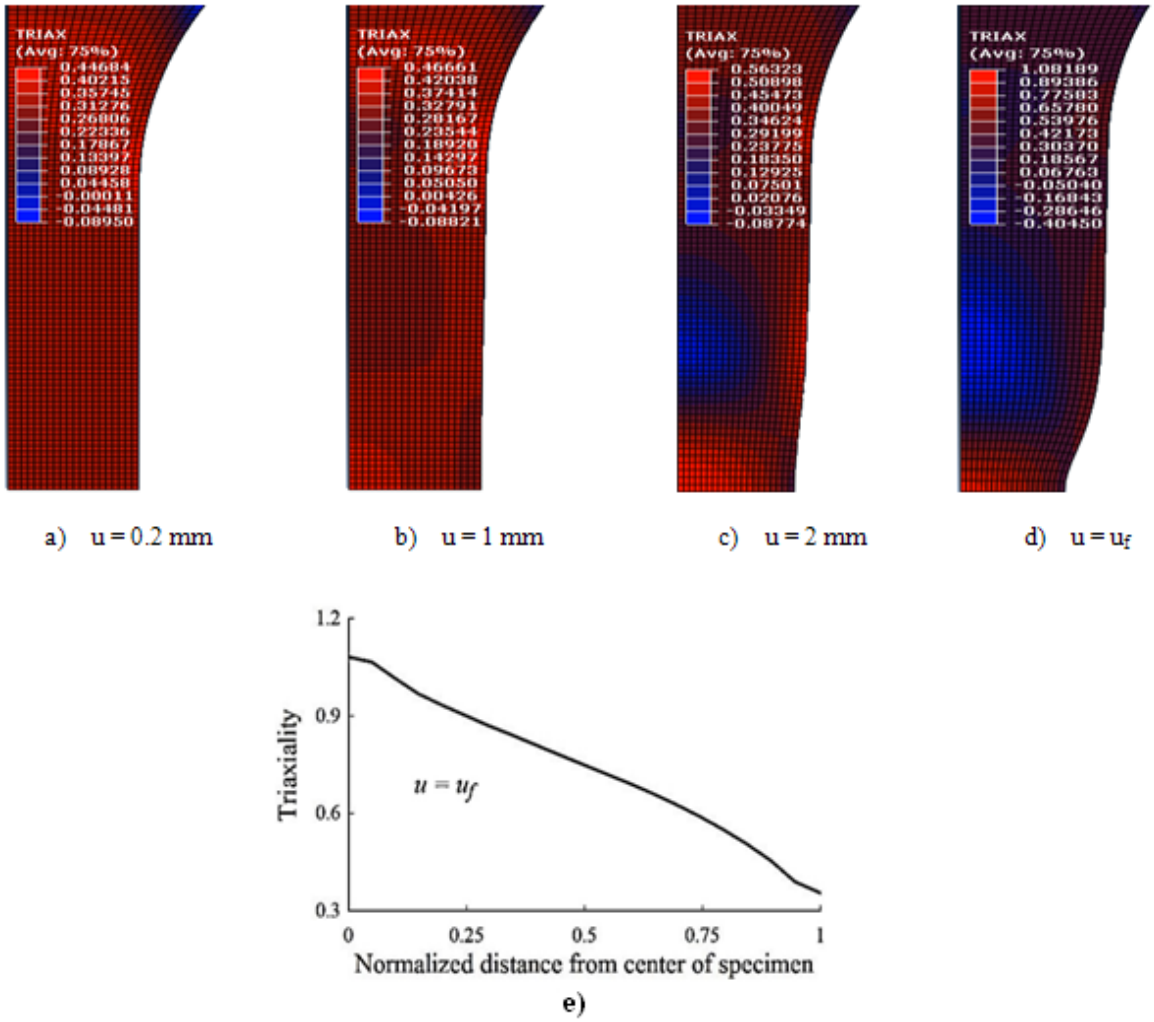

Fig. 12. a-d) Stress triaxiality contours at different displacements and, e) Stress triaxiality over the fracture surface at the onset of fracture.

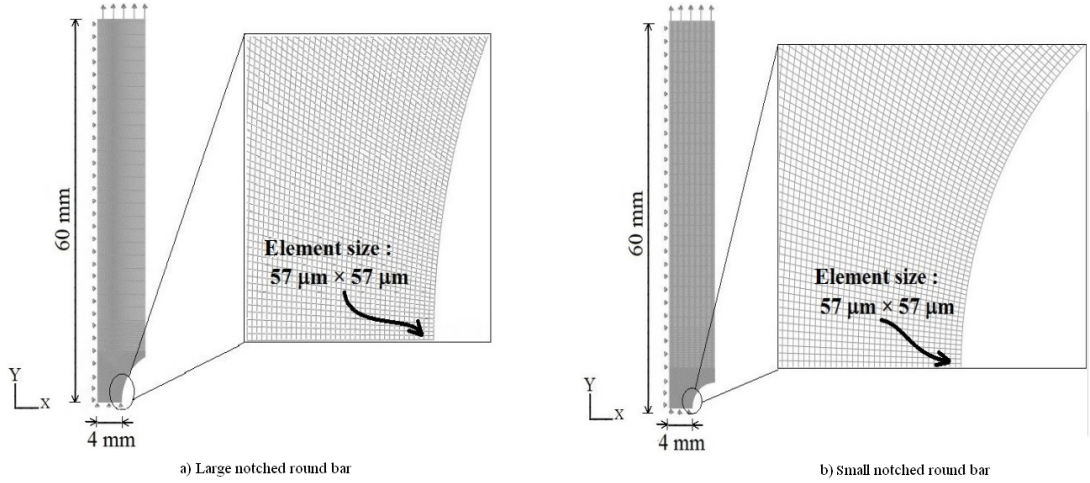

Fig. 13. Meshed models of notched round bars used in the Finite element simulation.

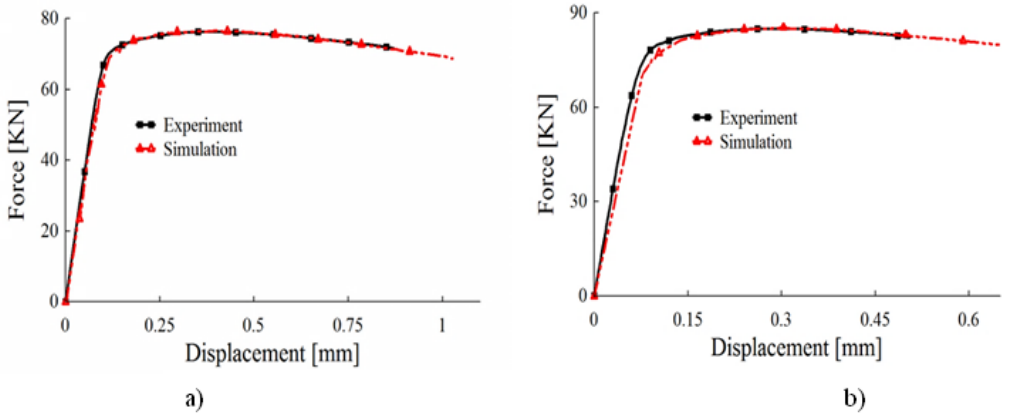

Fig. 14. Force-displacement curves of a) Large notched round bar and b) Small notched round bar.

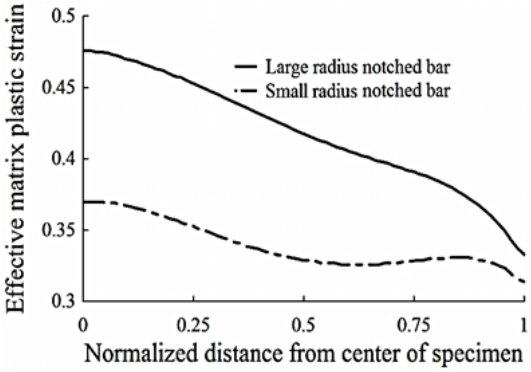

Fig. 15. Effective matrix plastic strain over the fracture surface at the onset of fracture.

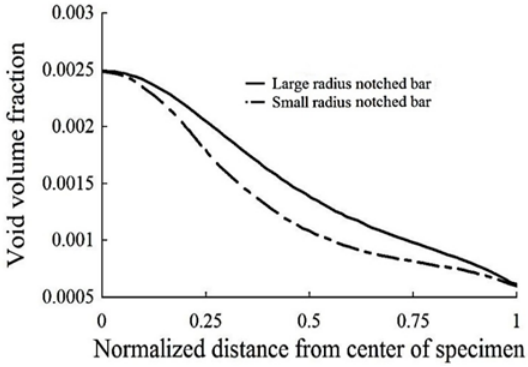

Fig. 16. Void volume fraction over the fracture surface.

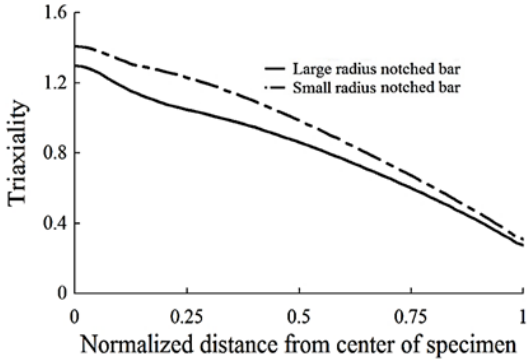

Fig. 17. Triaxiality over the fracture surface at the onset of fracture.

References

[1] F.A. McClintock, A criterion for ductile fracture by the growth of holes, J. App. Mech., 35 (1968) 363-371.

[2] J.R. Rice, D.M. Tracey, On the ductile enlargement of voids in triaxial stress fields, J. Mech. Phys. Solids., 17 (1969) 201-217.

[3] A.L. Gurson, Continuum theory of ductile rupture by void nucleation and growth: Part 1: Yield criteria and flow rules for porous ductile media, J. Eng. Mater. Technol., 99(1) (1977) 2-15.

[4] V. Tvergaard, Influence of voids on shear band instabilities under plane strain conditions, Int. J. Fract., 17(4) (1981) 389-407.

[5] V. Tvergaard, A. Needleman, Analysis of the cup-cone fracture in a round tensile bar, Acta. Metall., 32(1) (1984) 157-169.

[6] L. Xue, Constitutive modeling of void shearing effect in ductile fracture of porous materials, Eng. Fract. Mech., 75 (2008) 3343-3366.

[7] K. Nahshon, J.W. Hutchinson, Modification of the Gurson model for shear, Euro. J. Mech. A/Solids., 27 (2008) 1-17.

[8] Y. Bao, T. Wierzbicki, On fracture locus in the equivalent strain and stress triaxiality space, Int. J. Mech. Sci., 46(81) (2004) 81- 98.

[9] N. Bonora, D. Gentile, A. Pirondi, G. Newaz, Ductile damage evolution under triaxial state of stress: theory and experiments, Int. J. Plast., 21 (2005) 981-1007.

[10] G. Mirone, Role of stress triaxiality in elastoplastic characterization and ductile failure prediction, Eng. Fract. Mech., 74 (2007) 1203-1221.

[11] I. Barsoum, J. Faleskog, Rupture mechanisms in combined tension and shear experiments, Int. J. Solids Struct., 44 (2007a) 1768-1786.

[12] I. Barsoum, J. Faleskog, Rupture in combined tension and shear: micromechanics, Int. J. Solids Struct., 44 (2007b) 5481-5498.

[13] M. Brunig, O. Chyra, D. Albrecht, L. Driemeier, M. Alves, A ductile damage criterion at various stress triaxialities, Int. J. Plast., 24 (2008) 1731-1755.

[14] Y. Bai, T. Wierzbicki, A new model of metal plasticity and fracture with pressure and Lode dependence, Int. J. Plast., 24 (2008) 1071-1096.

[15] L. Driemeier, M. Brnig, G. Micheli, M. Alves, Experiments on stress-triaxiality dependence of material behavior of aluminum alloys, Mech. Mater., 42 (2) (2010) 207-217.

[16] A.S. Khan, H. Liu, A new approach for ductile fracture prediction on Al 2024-T351 alloy. Int. J. Plast., 35 (2012) 1-12.

[17] L. Malcher, F.M.P. Andrade, J.M.A., César de Sá, An assessment of isotropic constitutive models for ductile fracture under high and low stress triaxiality, Int. J. Plast., 30-31(0) (2011) 81-115.

[18] J. Lemaitre, A continuous damage mechanics model for ductile fracture, ASME J. Eng. Mater. Technol., 107 (1985) 83-89.

[19] Z. Voyiadjis, S.H. Hoseini, G.H. Farrahi, Effects of stress invariants and reverse loading on ductile fracture initiation, Int. J. Solids. Struct., 49(13) (2012) 1541-1556.

[20] Y. Bai, T. Wierzbicki, A comparative study of three groups of ductile fracture loci in the 3D space, Eng. Fract. Mech., 135 (2015) 147-167.

[21] G. Mirone, R. Barbagallo, D. Corallo, A new yield criteria including the effect of lode angle and stress triaxiality, Procedia. Struc. Integ., 2 (2016) 3684-3696.

[22] M. Ying-Song, S. Dong-Zhi, A. Florenc, Z. Ke-Shi, Influences of initial porosity, stress triaxiality and Lode parameter on plastic deformation and ductile fracture, Acta Mechanica Solida Sinica, 30(5) (2017) 493-506.

[23] C. Chu, A. Needleman, Void nucleation effects in biaxially stretched sheets, J. Eng. Mater. Tech., 102 (1980) 249-256.

[24] Y. Bao, T. Wierzbicki, A comparative study on various ductile crack formationcriteria, J. Eng. Mater. Tech. Trans. ASME., 126 (2004) 314-324.

[25] R. Narasimhan, A.J. Rosakis, B. Moran, A three-dimensional investigation of fracture initiation by ductile failure mechanisms in a 4340 steel, Int. J. Fract., 56 (1992) 1-24.